Comparative Accuracy Assessment of Nadir and Hybrid RTK-UAV Photogrammetry for Surface Detail Extraction

Alkan, M. N.
Hitit University, Osmancık Ömer Derindere Vocational High School, 19500, Çorum, Türkiye
E-mail: nurullahalkan@hitit.edu.tr
**Corresponding Author*

DOI: https://doi.org/10.52939/ijg.v22i7.5078

Abstract

This study evaluates the metric reliability of nadir and hybrid RTK-UAV photogrammetric models for surface detail extraction on a two-story building without using Ground Control Points (GCPs). Two photogrammetric models were generated: a standard model based only on nadir images and a hybrid model combining nadir, oblique, and manual façade-oriented images. Both models were assessed using terrestrial reference data obtained from GNSS and reflectorless total station measurements. The evaluation was performed at three levels: point-based, length-based, and surface-based comparisons. The point-based results indicate that the nadir model allowed 21 of the 35 reference points to be reconstructed, whereas the hybrid model allowed the 3D positions of all. The hybrid model also substantially improved vertical and overall 3D accuracy, reducing the ΔZ MAE from 0.355 m to 0.029 m and the 3D RMSE from 0.454 m to 0.046 m. In the length-based analysis, the nadir model was included where both endpoints of a selected linear element could be clearly identified. The nadir model allowed only 4 of the 14 selected length pairs to be measured, whereas the hybrid model allowed all 14 length pairs to be evaluated. On the other hand, the hybrid model had close agreement with the reference lengths, with a MAE of 0.012 m and RMSE of 0.016 m. Also, there is no statistically significant difference observed between reference and model lengths. In the surface-based comparison, the nadir model could represent only 4 of 7 reference surfaces, a limited number of reference surfaces, whereas the hybrid model enabled all selected surfaces to be evaluated, including upper-floor and under-eave regions. Although the nadir model produced lower average errors on some reconstructed surfaces, its limited surface coverage reduced its practical applicability. Overall, the findings demonstrate that hybrid RTK-UAV image acquisition provides a more robust and reliable solution than nadir-only acquisition for building surface documentation, particularly in façade areas with restricted visibility.

Keywords: Façade Documentation, GNSS-based Terrestrial Measurements, Hybrid Image Acquisition, Surface Detail Extraction, UAV Photogrammetry

1. Introduction

Over the last decade, photogrammetric applications based on Unmanned Aerial Vehicles (UAVs) have become an important data acquisition technique for map production, 2D/3D modelling, structural and archaeological recording, and remote sensing, with the advantage of reduced fieldwork duration. UAV-based photogrammetric point clouds can be enhanced using oblique imagery for improved 3D modeling [1]. Earlier studies also demonstrated the potential of high-precision and detailed data acquisition through low-altitude photogrammetric flights in complex sites. UAV systems have been used for large-scale mapping in archaeological sites, while UAV photogrammetry has also been explored for mapping and 3D modelling in archaeological and agricultural documentations [2] and [3]. The broader use of unmanned aerial systems background in photogrammetry and remote sensing has also been widely reviewed [4]. In addition, point clouds generated from multi-view and low-altitude UAV imagery can provide high precision metric data if the collected images are properly georeferenced and validated [5]. Also, quantitative assessment for metric applications by integrating GCPs into the scene for low-cost UAV outputs were emphasized [6]. However, the geometric quality of the final outputs depends on multiple factors, including image resolution, georeferencing strategy, image acquisition geometry, flight route diversity, and independent accuracy evaluation.

For engineering and construction applications, terrestrial verification of the derived 3D positions is crucial. In most UAV-based applications, Ground Control Points (GCPs) are established and measured with conventional techniques, such as GNSS and total station, to support bundle block adjustment and obtain high-precision coordinates of the target features. The number and spatial distribution of GCPs substantially affect photogrammetric model accuracy [7] and [8]. Ground control quality, quantity, and bundle adjustment configuration directly influence the reliability of UAV-SfM products [9]. In a similar context, photogrammetric and RTK-GPS methods were compared for surveying applications in terms of elevation accuracy by using several control points [10].

More recently, UAV platforms equipped with Real-Time Kinematic (RTK), Post-Processed Kinematic (PPK), and Inertial Measurement Unit (IMU) modules have reduced the need for dense GCP establishment by supporting direct georeferencing and overlapping ratios of the images. UAV blocks were tested with GNSS-supported aerial triangulation using no or a minimum number of GCPs in the area [11], whereas onboard RTK-supported UAV measurements were evaluated for direct georeferencing [12] and [13]. RTK/PPK UAV photogrammetry using differential corrections from multiple GNSS base stations was assessed for different flight altitudes [14]. RTK- and PPK-based methods were compared for mapping different surface types [15], while PPK- and GCP-supported UAV products were evaluated under challenging terrain conditions [16]. GCP distribution and checkpoint validation remain important even when RTK-GNSS UAV data are used for large-scale topographic mapping [17]. SfM accuracy was assessed in surveying and mapping applications, confirming that final accuracy depends on both the positioning and validation strategy [18]. However, previous studies also indicated that independent validation is still required even when RTK-supported approaches are used, particularly for vertical accuracy, façade measurements, and engineering applications based on check points or terrestrial observations. This issue was also emphasized in studies comparing direct georeferencing and GCP-based processing workflows [19][20][21][22] and [23].

UAV photogrammetry has also been used for building 3D model generation, façade and structural inspection, and extraction of metric information such as lengths and surface-related measurements. Close-range UAV images were used for façade inspection [24], while the contribution of nadir and oblique images for building knowledge extraction and metric information was evaluated [25]. UAV imagery can also be used for 3D building modelling, façade evaluation, BIM registration, and integrated architectural documentation. The use of UAV images for building and 3D model generation was demonstrated and compared with conventional observation methods [26], UAVs were discussed as efficient tools for industrial façade inspection [27], and integrated surveying approaches for architectural and archaeological documentation using UAVs and laser scanning were presented [28]. UAV images can also be registered to BIM-related spatial models for building façade inspection with generalized Hough transformation (GHT) [29]. In addition, UAV photogrammetry was integrated with a deep-learning-based method for building extraction and floor area estimation, showing that UAV-derived data can support building-scale information extraction in addition to visual documentation [30]. However, these previous studies mostly focused on general model quality, positional accuracy, or task-specific measurements.

On the other hand, image acquisition strategy is one of the main factors affecting the quality of 3D models. The standard nadir-imagery approach is efficient for open areas, roofs, and horizontal surfaces, but it may remain weak when the target is a building with vertical façades, window surroundings, and regions beneath the eaves. Flight altitude can affect the spatial accuracy of UAV-derived products, indicating that acquisition parameters should be considered together with camera viewing geometry [31]. The limitations of nadir-only imagery are also related to incidence angle and ray intersection geometry around vertical surfaces. In nadir-only image blocks, vertical surfaces are often reconstructed under weak or unfavorable viewing geometry, especially when surfaces are observed at oblique or grazing angles. For this reason, image rays may have weak convergence on vertical surfaces, and tie points between images may become sparse or unstable. This situation can lead to larger uncertainties in the vertical components of reconstructed building details. Therefore, weak image geometry can become a major issue even if the UAV platform has an RTK/IMU module and this situation may limit vertical surface reconstruction.

To cope with these issues, oblique and façade-oriented images are generally used to increase viewing-angle diversity, improve ray convergence, and provide additional image support for vertical surfaces. Previous studies using oblique UAV imagery indicated that the reconstruction of façades and surface details can be improved in terms of 3D modelling, length-area-volume measurements, and point-cloud-based surface quality assessment. The accuracy of UAV-derived 3D photogrammetric models was assessed, emphasizing the need to evaluate model quality in addition to visual appearance [32], and photogrammetric model quality for façade and building reconstruction using an RTK-UAV was evaluated by comparison with terrestrial measurements [33]. Three-dimensional models generated from UAV oblique images were examined [34], while the potential of UAV photogrammetric point clouds for façade detection and 3D building reconstruction was investigated [35]. A point-cloud-based system for surface quality evaluation of buildings was proposed [36], and metric measurement accuracy in UAV-based oblique photogrammetry with or without GCPs was evaluated [37]. UAV flight parameters for heritage façade inspection, particularly on vertical surfaces, were also examined [38]. However, using oblique or façade-oriented images has some disadvantages, including increased image acquisition time, need for UAV operator proficiency, more complex image block geometry, additional processing workload, and variability in point cloud density. Moreover, improved surface reconstruction does not automatically guarantee lower metric errors. Therefore, a hybrid oblique–nadir–façade-oriented image acquisition strategy should be evaluated not only in terms of visual completeness, but also in terms of whether it provides measurable and accurate surface information.

Previous studies have investigated georeferencing strategies and image acquisition approaches, but a practical gap remains in the evaluation of UAV-derived building models. These studies mainly focused on positional accuracy, RTK/GCP performance, overall 3D model quality, or individual measurement tasks. Although these studies provide important evidence on GCP distribution, RTK/PPK positioning, flight altitude, oblique imagery, and building extraction, they generally do not evaluate point reproduction, length measurement, and planar surface representation together within the same building-scale validation framework. Fewer studies have evaluated the same building under the same experimental framework, to figure out if a reconstructed photogrammetric model can model reference façade points, provide reliable linear measurements, and represent planar surfaces. This is still an important issue, particularly for upper-floor and under-eave areas, where nadir imagery is geometrically limited and the quality of the reconstructed model may depend strongly on the image acquisition strategy.

To address this gap, this study compares two different RTK-UAV photogrammetric workflows applied to the same two-story building without GCP establishment: (i) a conventional nadir-only image acquisition strategy and (ii) a hybrid strategy combining nadir, oblique, and façade-oriented images. These models were evaluated using independent terrestrial reference data and accuracy assessment was conducted at three complementary levels: point-based coordinate comparison, length-based comparison of selected building elements, and surface-based planar evaluation. This multi-level framework enables the evaluation of geometric errors, reconstruction completeness, and practical measurability in façade regions that are difficult to model using only nadir images.

This study also tests three specific claims, whether: (i) the hybrid workflow increases the number of measurable façade points and reconstructed vertical surfaces compared with nadir imagery; (ii) additional oblique and façade-oriented images reduce 3D errors caused by weak nadir geometry; and (iii) improved 3D model reconstruction involves a trade-off with local surface error metrics in more complex and occluded façade areas. With this workflow, this study intends to provide a practical and testable evaluation of nadir-only and hybrid RTK-UAV imagery for building surface detail extraction.

2. Methodology

2.1 Study Area and Building Characteristics

This study was conducted on a two-story main building located on the Osmancık campus of Hitit University. The building presents a geometry well suited to photogrammetric assessment in terms of flat wall surfaces, window openings, upper-floor details, and areas located beneath the eaves. The height to the underside of the eaves is approximately 6.5 m, and the total enclosed area of the building is approximately 6500 m² (Table 1). The measurements focused particularly on façade details located on three different faces within the U-shaped courtyard on the northern side of the building.

This test building was selected because its U-shaped courtyard on the north wing has upper-floor façades, window openings, and eaves which create a controlled but challenging visibility condition for nadir and hybrid UAV image acquisition. Geometric properties of the structure are important because façade orientation, eave depth, and wall height directly affect image visibility, ray intersection geometry, and the ability of nadir and oblique images to reconstruct vertical surfaces. Although the selected building provides a suitable test case for comparing nadir-only and hybrid image acquisition

ISSN: 1686-6576 (Printed) | ISSN 2673-0014 (Online) | © Geoinformatics International

strategies, the experimental design is limited to a single building with a specific U-shaped plan, façade texture, roof geometry, eave configuration, and campus environment. Therefore, the results should be interpreted in relation to this particular architectural and environmental setting. The findings may not be directly transferable to buildings with different urban occlusion conditions without additional validation.

Distinct detail points on the building surfaces, together with virtually defined planar surface panels, were used in the evaluation (Figure 1). At the upper-floor level, the eave structure restricts the visibility of wall surfaces; therefore, these regions were considered as the areas where the most pronounced differences between alternative data acquisition strategies could be observed [5][34] and [38]. For this reason, the building was regarded as a suitable test site for point-, length-, and surface-based comparisons.

2.2 Terrestrial Reference Measurements

The reference dataset was established using a combination of GNSS and total station measurements in this study. The 3D coordinates traverse network was measured using a Spectra SP80 GNSS receiver, and the façade detail points were observed using a Spectra Focus 8 total station. According to the manufacturer specifications, the GNSS receiver provides a positioning precision of 8 mm+0.5 ppm in the horizontal and 15 mm+0.5 ppm in the vertical components under Network-RTK observations. The total station has an angular accuracy of 2’’ and a reflectorless distance measurement accuracy of ± (3+2 ppm x D) mm. These specifications were considered as sufficient for establishing an independent terrestrial reference network for the evaluation of UAV-derived surface features (Table 2).

Table 1: Geometric characteristics of the test site and evaluated façades

Parameter	Metrics
Building center coordinates	34.78° E / 40.99° N
Building plan type	U-shaped, two-story educational building
Enclosed area	~6500 m^2
Eave underside height	~6.5 m
Floor height	~3.25 m
Main plan dimensions	~53 m x 76 m
Courtyard dimensions	26 m – 27 m - 17 m (west-south-east)
Eave overhang depth	~0.80 m
Evaluated façade orientations	Façade 1&3 – North-south (~180°) Façade 2 – West-east (~90°)
Occlusion sensitive regions	Upper floor, under eave regions, window surroundings

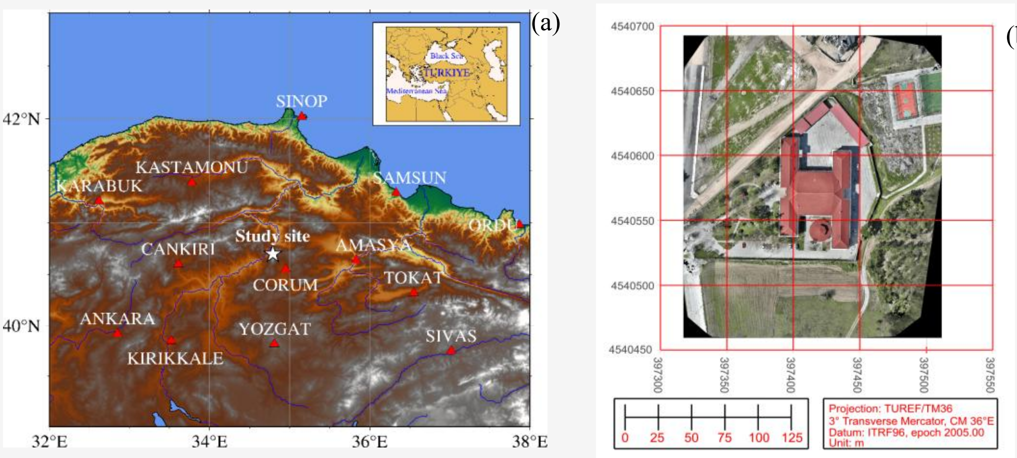

Figure 1: Location and spatial characteristics of the test building: (a) regional location map, where the white star represents the position of the test site, and (b) ortho-mosaic view of the test site and selected façades of the building (blue). Projected coordinates in (b) are presented in the TUREF/TM36 coordinate reference system (3° Transverse Mercator; central meridian 36°E; units: m). The regional location map in panel (a) was generated using Generic Mapping Tools (GMT) [48]

Table 2: Technical specifications of the terrestrial reference measurement instruments

Instrument	Model	Role in the study	Precision
GNSS Receiver	Spectra SP80	Measurement of traverse point coordinates	Hor.: 8 mm+0.5 ppm Ver.: 15 mm +0.5 ppm
Total station	Spectra Focus 8	Reflectorless façade/detail measurements	Angle: 2’’ Distance: ±(3+2 ppm x D) mm

Three traverse points were established in the field, and their coordinates were determined by averaging the results obtained from two separate GNSS observation sessions carried out at one-hour intervals. Data were collected at a 1 s logging interval, with 180 epochs recorded in each session. The traverse points obtained in this way subsequently served as control points for the reflectorless total station measurements. The 3D coordinates of the traverse points were computed in a 3° Transverse Mercator projection with a central meridian of 36°E in the northern hemisphere and referenced to the ITRF96, epoch 2005.00 datum. The 3D coordinates of the detail points on the building surfaces were obtained by using reflectorless total station measurements. In this context, window corners, pairs of points representing selected linear elements, and points used to define planar surfaces were measured. The 3D coordinates of these features were used as independent terrestrial reference data to evaluate the accuracy of the point-, length-, and surface-based data derived from the photogrammetric models (Figure 2).

2.3 UAV Data Acquisition

DJI Mavic 3 Enterprise UAV with a 20 MP camera and RTK module was used in the photogrammetric data collection. The platform provides cm-level positioning support through solutions such as Network RTK, Custom Network RTK, and the D-RTK 2 Mobile Station [39] and [40]. The RTK/PPK-based 3D camera position of the UAV platform can be incorporated into the photogrammetric bundle block adjustment as initial exterior orientation data to support direct georeferencing of the model. Actual positional performance, time synchronization with the RTK module, IMU effects, flight geometry, and the processing strategy are also of critical importance for the reliability of the georeferencing process [14][18][20] and [32].

During the UAV image acquisition, RTK corrections were provided from a local GNSS base receiver established near the center of the flight area. The coordinates of the base receiver were determined using the TUSAGA-AKTIF (CORS-TR) system. The maximum distance between the UAV and the local base receiver was approximately 300 m during the flights. According to the flight logs the RTK solution remained fixed during the whole mission, and approximately 10 GPS and 10 GLONASS satellites were tracked, therefore, the camera positions obtained from the RTK-supported UAV system were used as direct georeferencing information in the photogrammetric processing. UAV data were collected and processed using two different approaches. The first processing workflow included a standard photogrammetric model which was generated using only nadir images. In the second workflow, in addition to the nadir images, complementary façade images acquired from oblique and manual flights were incorporated together to form a hybrid photogrammetric model (Figure 3).

For both autonomous acquisitions, the flight altitude was selected as 40 m due to physical obstacles around the study area and flight safety constraints, while the forward and side overlap ratios were applied as 80% and 70%, respectively. RTK-supported positioning information from the UAV was used in both flights, and no GCPs were established. This approach was selected because the RTK/PPK-based direct georeferencing can provide acceptable horizontal accuracy in some applications. However, validation using independent terrestrial reference measurements is still recommended, particularly for the vertical component [10][19][20] and [35] (Table 3). During this study, the flight altitudes were fixed at 40 m for the autonomous nadir and oblique image acquisitions. This height was selected as a practical compromise between image resolution, obstacle avoidance, safe flight operation, and sufficient coverage of the selected façades. The test building has a U-shaped courtyard, upper-floor façade surfaces, eave overhangs, and nearby obstacles (terrain, trees, etc.) that restrict and risk low-altitude flights. A lower altitude, such as 30 m, could potentially improve the GSD, but it would also increase the number of required images, flight duration, processing workload, and collision risk around the area. Conversely, higher altitudes, such as 50 m or 100 m, would provide wider coverage but would increase the GSD and reduce the visibility of small façade details. Since the aim of this study was to compare nadir-only and hybrid acquisition geometries under the same height condition, flight altitude was kept constant and was not tested as an independent variable.

Figure 2: Measured features using terrestrial techniques. Wall surfaces 1, 2, and 3 located on the northern wing of the building are presented with (a), (b) and (c), respectively. Observed data are illustrated as orange triangles for points, yellow lines for lengths, and green rectangles for surfaces. The surfaces located close to the roof and beneath the eaves on building surfaces 2 and 3 (surfaces 2, 5, and 7) could not be reconstructed in the nadir photogrammetric model

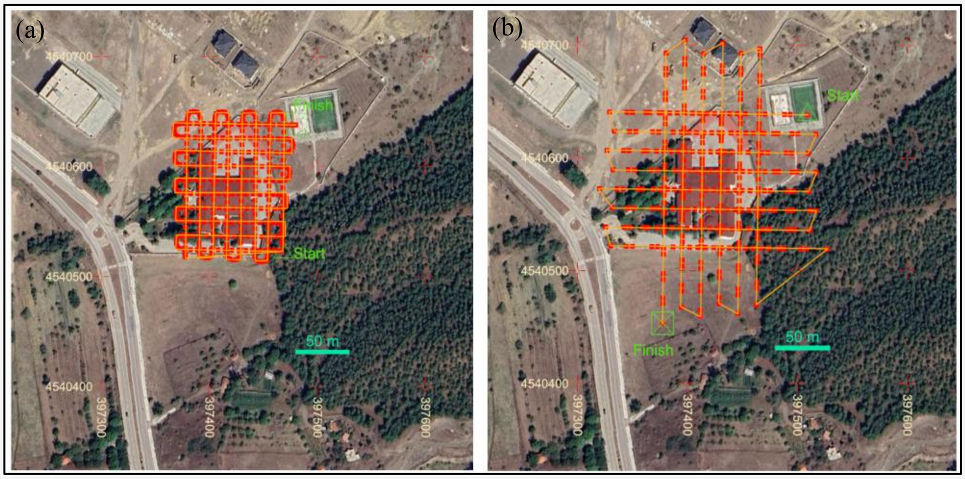

Figure 3: Autonomous flight routes for generating photogrammetric models. The nadir-model (a) and hybrid model flight routes are given, respectively. The take-off (start) and landing (finish) points of the UAV platform are also indicated in both figures. Each image acquisition position of the platform is represented by a red square, and each flight strip is shown by orange lines. For the hybrid model, the flight route is noticeably longer in the north–south and east–west directions than that of the nadir model in order to enable the acquisition of site images at a 45° oblique angle

Table 3: Technical properties of the autonomous flights by using the DJI Mavic 3E UAV platform. All image acquisition datasets were processed with an RTK fixed solution and RTK corrections were received from a local GNSS base receiver, which coordinates were determined using the TUSAGA-AKTİF (CORS-TR) system. During the flights, approximately 10 GPS and 10 GLONASS satellites were available

Dataset	Data Acquisition Mode	Flight Altitude/Façade Distance	Camera Orientation	Planned Overlap/Coverage Strategy	GSD	Number of Images
Nadir Model	Autonomous	40 m	Nadir imagery	80% forward overlap 70% side overlap	0.8 cm	437
Hybrid Model – Nadir Subset	Autonomous	40 m	Nadir imagery	80% forward overlap 70% side overlap	Part of the hybrid model average GSD: 1.7 cm	58
Hybrid Model – Oblique Subset	Autonomous	40 m	45° oblique imagery	80% forward overlap 70% side overlap	Part of the hybrid model average GSD: 1.7 cm	286
Hybrid Model – Manual Façade Subset	Manual	~25 m from façades ~5 m flight altitude	Façade-oriented manual imagery	Visual multi-view coverage of the selected façade details and under-eave regions	Part of the hybrid model average GSD: 1.7 cm	8

2.3.1 Nadir flight

The nadir flight was conducted to represent the standard photogrammetric data acquisition approach in this study. In this context, the area of interest was imaged using autonomous flight routes planned in the north–south and east–west directions. The camera was set to a 90° position to provide a nadir viewing geometry, and this dataset was used to model only the surfaces visible from above and the general building geometry. The model generated from these images was referred to in the study as the “nadir model” and was used as the baseline comparison model for the other data acquisition approach. The nadir dataset consisted of 437 images and had an average GSD of 0.8 cm.

2.3.2 Oblique and free-flight acquisition

For the hybrid photogrammetric model, the second UAV flight initially involved the collection of nadir and 45° oblique images through an autonomous flight mission, where this was selected as the default oblique acquisition setting of the flight application. Acquisition angle 45° was not tested as an independent variable; rather, it was selected heuristically to increase the visibility of vertical façades and under-eave regions while maintaining sufficient coverage of the roof and upper building geometry. Subsequently, additional images were captured by manual flight in order to achieve a better representation of the three selected façades of the building and the areas located beneath the eaves. These images were used specifically to support regions with limited visibility in the nadir flight, such as upper-floor surfaces, window surroundings, and the undersides of the eaves. In this way, the hybrid model was constructed as a dataset, which is capable of representing not only the visible geometry from above, but also façade surfaces and occluded areas more effectively [5][34] and [33]. The average GSD of the hybrid model was 1.71 cm. Although this value was larger than that of the nadir-only model, the hybrid dataset provided additional viewing directions and improved façade visibility, which were critical for reconstructing upper-floor and under-eave details. The manual image acquisition was conducted on the three selected northern façade zones used in the evaluation. During the flight, the UAV was flown approximately parallel to the façades at an average distance of about 25 m and at a flight height of ~4-5 m, so that the camera could observe the upper-floor and under-eave regions that were weakly visible in the nadir-only dataset. Since the manual acquisition was not based on programmed overlap ratios, adequate coverage was ensured by acquiring multiple façade-oriented images with visual overlap and convergent viewing geometry.

During the manual image acquisition, the camera was oriented toward the façade surfaces and under-eave regions. Therefore, there were small variations in viewing direction according to the visibility of the target façade details. The operator followed a systematic façade-parallel route along the three selected northern façade zones which expands from east-west direction, but the image capture was also adjusted adaptively where the eave structure, window surroundings, or local occlusions limited visibility. Consistency between the manually acquired images was maintained by keeping an approximately constant façade distance of about 25 m, using a similar flight height of approximately 4–5 m, and ensuring that each selected façade detail was visible in more than one image. Adaption with the nadir-oblique imagery of the photogrammetric model requires common points visible from the autonomous flight route, and manual acquisition was conducted under the condition to capture the most details available.

As a result, the hybrid photogrammetric model had a separate image dataset by combining autonomous nadir (58), autonomous oblique (286), and manual façade-oriented images (8). Here, the hybrid dataset contained fewer images than the nadir-only dataset because it was not created by adding all nadir-model images to the oblique and manual images. Instead, it was generated as a separate and more targeted acquisition set that included a smaller nadir subset, a larger number of oblique images, and a limited number of manual façade-oriented images. The main accuracy improvement approach in this study is the enhancement of the image acquisition geometry rather than a shift in the photogrammetric processing algorithm. The hybrid model was designed to increase the visibility and image coverage of the façade surfaces, upper floor details, and features that were poorly reconstructed in the nadir-only dataset. By constructing a hybrid model including nadir-oblique-manual façade digital images, the model was expected to provide stronger image intersection, denser point cloud specifically on vertical surfaces, and better reconstruction of the surfaces affected by occlusion where the nadir and autonomous oblique images had limited visibility.

It should also be noted that the hybrid workflow combines autonomous and manual image acquisition. Therefore, the improvement observed in the hybrid model should be interpreted as the combined effect of adding oblique and targeted façade-oriented images, rather than as the effect of a fully autonomous acquisition strategy alone. The manual component may introduce operator dependency and reduce direct reproducibility compared with the nadir-only workflow. Before photogrammetric processing, the oblique and manual images were visually inspected for image blur, motion artifacts, and improper exposure. Images with severe blur, strong motion artifacts, or inadequate exposure were planned to be excluded from the dataset, but none of the imagery was rejected after this inspection.

2.4 Photogrammetric Processing

Acquired images for both flight routes were evaluated as separate data groups. The first group consisted of the photogrammetric model generated using only nadir images, whereas the second model comprised the hybrid dataset in which images acquired from nadir, oblique, and manual flights were used together. For both models, software packages such as Pix4D, Agisoft Metashape, and 3DF Zephyr can be used for image matching, determination of exterior orientation parameters, dense point cloud generation, and model reconstruction [35][41][42] and [43]. The first software was selected for processing, which enabled the two datasets to be compared under the same workflow. Both the nadir and hybrid datasets were processed using the same general processing configuration. The RTK-supported image positions were used for direct georeferencing, and no 3D GCPs were used in the bundle block adjustment (Table 4).

Table 4: Photogrammetric processing parameters used for the nadir and hybrid models

Processing Stage	Parameter	Setting
Camera model	Camera model	M3E_12.3_5280x3956 (RGB)
Coordinate system	Image coordinate system	WGS84
	Output coordinate system	TUREF/TM 36
Georeferencing	Camera position source	RTK-supported UAV image positions
	GCP use in bundle adjustment	No 3D GCP used
Initial processing	Processing template	3D maps
	Keypoints image scale	Full, image scale
	Matching image pairs	Aerial grid or corridor
	Geometrically verified matching	No
Camera calibration	Calibration method	Standard
	Internal parameter optimization	All
	External parameter optimization	All
Point cloud densification	Image scale	1/2 image size
	Point density	Optimal
	Minimum number of matches	3
3D textured mesh	Mesh resolution	Medium
DSM and orthomosaic	Resolution	1xGSD
	Noise filtering	Applied
	Surface smoothing	Applied (sharp)

In order to transform the coordinates of the photogrammetric models into a terrestrial global coordinate system, the RTK-supported positioning information of the UAV platform was used. Accordingly, the exterior orientation parameters of the images were obtained through a direct georeferencing approach, and 3D positions were computed for both models in the ITRF datum and the TUREF/TM36 3° Transverse Mercator projection system. Subsequently, point-, length-, and surface-based assessments were carried out on the corresponding photogrammetric models to evaluate the accuracy of both approaches (Figure 4). The initial camera parameters read from the image metadata were used as starting values, and camera self-calibration was performed during bundle block adjustment in this study. The calibration method was set to standard, and all internal and external camera parameters were optimized. This approach allowed the focal length, principal point coordinates, radial distortion parameters, tangential distortion parameters, and exterior orientation parameters to be refined within the same bundle adjustment (Table 5). The overall photogrammetric processing quality was also evaluated using the standard quality indicators and reported for both the nadir and hybrid image blocks in order to verify that the observed differences between the two models were mainly related to acquisition geometry rather than processing artifacts.

The low mean reprojection for both models indicates that the image blocks were adjusted consistently after self-calibration. Lens distortion and camera geometry effects were estimated and compensated during the bundle adjustment process. Since the same camera model and calibration strategy were used for both datasets, the comparison between the nadir and hybrid models was not affected by different camera calibration procedures. In addition, both image blocks had a 100% image calibration rate and cm-level geolocation residuals which indicates that the photogrammetric processing quality of both models was comparable. Therefore, the differences observed in point-, length-, and surface-based accuracy were interpreted mainly as the effect of image acquisition geometry and façade visibility rather than as a consequence of processing artifacts.

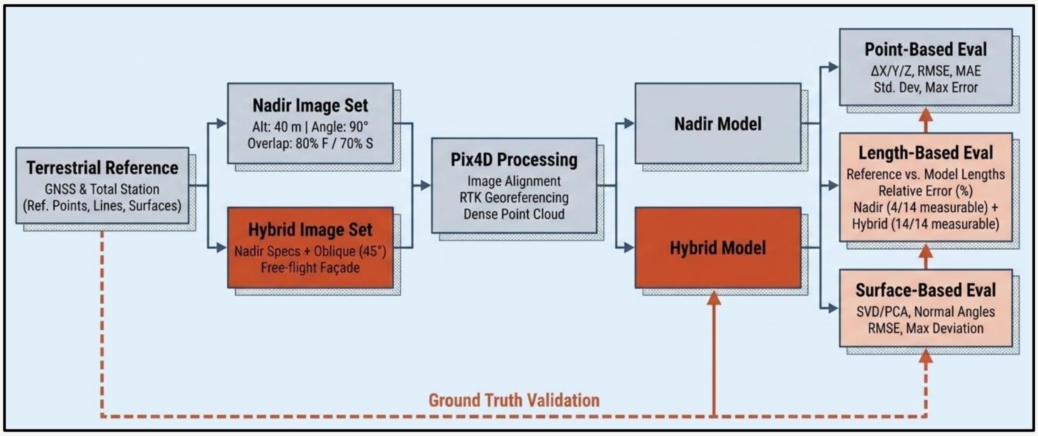

Figure 4: Workflow of data acquisition and processing strategies in this study

Table 5: Camera self-calibration and photogrammetric quality indicators

Quality Indicator	Nadir Model	Hybrid Model
Camera model	M3E_12.3_5280x3956 (RGB)	M3E_12.3_5280x3956 (RGB)
Calibration approach	Self-calibration	Self-calibration
Pre-calibration used	No	No
GCP in bundle adjustment	No	No
Number of calibrated images	437/437	352/352
Number of geolocated images	437/437	352/352
Average GSD	0.8 cm	1.7 cm
Camera optimization difference	3.99%	2.81%
Mean projection error (pixel)	0.182	0.187
Absolute camera uncertainty (mean X/Y/Z)	0.003 / 0.003 / 0.002 m	0.005 / 0.005 / 0.006 m
Relative camera uncertainty (mean X/Y/Z)	0.002 / 0.002 / 0.003 m	0.002 / 0.002 / 0.002 m
Geolocation RMS error (X/Y/Z)	0.008 / 0.009 / 0.008 m	0.013 / 0.015 / 0.011 m

Both datasets were processed as independent projects with the same photogrammetric processing strategy in order to ensure comparable conditions. The difference between the two models was limited to image acquisition geometry, and all other processing conditions were kept as constant. Also, no model-specific manual editing was applied to the dense point clouds. The comparison and evaluations based on points, lengths, and surfaces were conducted under the same reference coordinate system and error metrics. For point-based comparison, an additional common-point analysis was also performed using only the points that could be reconstructed in both models to allow a direct comparison under same conditions. Therefore, the reported differences between the nadir and hybrid models were interpreted primarily as the effect of acquisition geometry and façade visibility rather than differences in photogrammetric processing configuration.

Previous studies indicate that photogrammetric models generated from nadir images may be insufficient for representing certain areas with limited visibility, whereas hybrid data acquisition approaches can provide a more complete surface representation in such regions [5][33] and [34]. Similarly, in this study, the model generated from nadir imagery was also inadequate to represent the above-mentioned regions. By contrast, the hybrid model provided a more comprehensive surface representation. Therefore, the photogrammetric processing steps were considered not only for model generation but also for evaluating the effectiveness of different data acquisition geometries in representing building details (Figure 5). Figure 5 demonstrates the point cloud view of the hybrid photogrammetric model and the locations of the photogrammetric features selected for geometric comparison. The green cone markers indicate the points used in the point- and length-based comparison, and the brown markers represent the points used to define the planar wall surfaces. Figure also illustrates the spatial distribution and type of the selected compared features, and the sufficient visual and geometric representation of the interested details were provided by the hybrid model.

Figure 5. Enhanced point cloud view data of surfaces 1, 2, and 3 generated from the hybrid photogrammetric model: (a) Surface 1 heading east, (b) surface 2 heading north, and (c) surface 3 heading west are represented respectively. The green markers indicate the detail points used in the point- and length-based comparisons, whereas the brown markers indicate the representative points selected for the surface-based comparison. Approximate local scale indicators were added using known façade distances between clearly identifiable reference points on the same wall plane

2.5 Point-based Comparison Procedure

This comparison was based on the evaluation of the corresponding points from the photogrammetric models for which 3D coordinates had been measured by terrestrial measurements and defined as reference data. For this purpose, residuals were evaluated for the points which were reconstructed from the nadir and hybrid models, and the horizontal and vertical accuracy behavior of each model was examined separately.

The corresponding points were identified manually on the dense point cloud and image-supported model view. Each point was selected first by visually locating the closest representative point for the corresponding terrestrial detail, then manually marked by using at least 3 different images for the same feature and adjusted by considering the location errors. The same operator performed the feature identification for both the nadir and hybrid models using the same procedure in order to reduce operator-related inconsistency. For each reference point, the corresponding photogrammetric point was selected only when the detail was clearly visible and could be interpreted consistently on the model. This procedure was especially important and time consuming for the nadir model, where several upper-floor points could not be identified reliably. It should also be noted that the manual point identification on a dense point cloud may introduce an additional uncertainty for the estimated 3D positions, which might reach to cm-level specifically around the under-eave regions in terms of point density and surface continuum. Therefore, point-based errors include photogrammetric reconstruction errors and potential effects of manual feature identification were also reported in this study, and was considered when interpreting the point-based comparison results.

Each reference point measured by terrestrial methods and paired with their corresponding photogrammetric model pair and coordinate residuals were computed using Equations 1 to 3:

$$\Delta X_i = X_{ri} - X_{pi}$$

Equation 1

$$\Delta Y_i = Y_{ri} - Y_{pi}$$

Equation 2

$$\Delta Z_i = Z_{ri} - Z_{pi}$$

Equation 3

Where ΔX_i, ΔY_i and ΔZ_i represent the coordinate differences between terrestrial and photogrammetric model data for each i-th feature on the building surface, respectively, and were used to evaluate the horizontal and vertical accuracy behavior of both nadir and hybrid models. The horizontal error (eH_i) and 3D error ($e3D_i$) for each point feature were calculated using Equations 4 and 5, respectively:

$$eH_i = \sqrt{\Delta X_i^2 + \Delta Y_i^2}$$

Equation 4

$$e3D_i = \sqrt{\Delta X_i^2 + \Delta Y_i^2 + \Delta Z_i^2}$$

Equation 5

In addition, the error magnitudes of the two- and three-dimensional coordinate residuals were also calculated to evaluate the overall positioning performance of the models. For each coordinate component, mean signed error, mean absolute error (MAE), root mean square error (RMSE), standard deviation, and maximum absolute error were calculated. Here, error metrics were used to evaluate:

- Mean signed error: Possible systematic bias
- MAE: Average error magnitude
- RMSE: Quadratic error magnitude
- Standard deviation: Dispersion of the residuals
- Maximum absolute error: Largest individual deviation.

Furthermore, to enable a comparison of the two models under equivalent conditions, an analysis using only the common points that could be reconstructed in both models was conducted. This approach was selected to reduce the potential bias arising from the different number of points produced by the nadir and hybrid models and to obtain directly comparable error metrics. This point-based coordinate evaluation using terrestrial observations is a direct validation approach for UAV photogrammetry at building documentation procedures, and same approach adopted to this study in order to assess both models in terms of reproducing the measured façade points precisely.

2.6 Length-based Comparison Procedure

In the initial evaluation, the nadir model was not considered for length-based assessment. The interested measurements need at least 2 points to be monitored, but nadir model did not allow to produce 3D positions of all the points. However, to preserve the comparative structure of the study, nadir-derived lengths were also calculated wherever both endpoints of a selected linear element could be reliably identified. If one or both endpoints of a selected

ISSN: 1686-6576 (Printed) | ISSN 2673-0014 (Online) | © Geoinformatics International

linear element could not be identified due to missing geometry, occlusion, or noisy reconstruction, the corresponding length was not computed. Both ends of the linear elements were manually identified on the dense point cloud and image-supported model view. No automatic snapping to point cloud vertices, mesh edges, or image features were applied. Instead, each point was selected by visually locating the same physical detail measured in the reference dataset. To reduce selection ambiguity, the operator used the RGB point cloud together with the available image projections and selected points only when the same feature could be interpreted consistently. The same operator performed the endpoint selection for both the nadir and hybrid models with the same procedure. It should be noted that this manual endpoint identification may introduce operator dependent uncertainty into the length-based comparison, therefore, length values were calculated only when both endpoints could be clearly identified. This procedure was adopted to avoid producing misleading length values from poorly defined photogrammetric features.

For each selected point pair, the three-dimensional Euclidean distance was calculated using reference and corresponding photogrammetric coordinates. The signed length difference and statistical tests were computed as the residual of these values. This approach allowed the nadir model to be quantitatively evaluated without excluding its weak performance in terms of feature availability.

2.7 Surface-based Comparison Procedure

The surface-based comparison procedure examined selected planar wall panels on the building which could be evaluated in both reference and photogrammetric models. A total number of seven surfaces were selected on the northern façades of the building, representing both the lower and upper floor regions. For each surface, a reference plane was fitted using the terrestrial reference points measured by total station. The number of reference points used to define the reference surfaces varied between 9 and 12 depending on the panel. In this study, a surface was considered comparable in a photogrammetric model only if the corresponding wall panel was visually identifiable in the dense point cloud and image-supported model view. At least five non-collinear and spatially distributed points selected to form a surface. These points were required to be located on the wall surface itself and not in locally noisy mixed-surface areas. The comparability decision was based on the availability of a continuous and interpretable surface patch and the ability to select at least five representative surface points distributed over the panel.

For the construction of reference and photogrammetric model panels, an SVD/PCA-based orthogonal least-squares plane fitting approach was used. This approach minimizes the sum of the squared perpendicular distances from the selected points to the fitted plane and provides the plane normal vector [44]. Here, a minimum number of three non-collinear points is sufficient for definition; however, at least five individual points were used for the photogrammetric surfaces in order to provide redundancy and to reduce the effect of local points selection uncertainty. The selected points were distributed across the surface panel as much as possible and no automatic plane segmentation, RANSAC-based outlier removal, or iterative reweighting was applied, because the evaluation designed as a controlled representative point-based comparison between reference and model surfaces. Therefore, outlier control was performed at the point selection stage rather than through an automatic robust fitting algorithm, and selected as controlled representative points from the same planar wall panel in order to provide comparable surface samples for the nadir and hybrid models. The RGB dense point cloud and image-supported model view were also used together to verify that the selected points belonged to the same physical wall surface. If five reliable and spatially distributed points could not be selected because of missing geometry, occlusion, or noisy reconstruction, the corresponding surface was recorded as not comparable.

Distances from the photogrammetric model points to the corresponding reference plane were calculated and the mean signed deviation, MAE, RMSE, standard deviation, and maximum absolute deviation were computed for each surface. In addition, the angle between the normal vectors of the reference and photogrammetric planes was computed to evaluate the orientation difference between the fitted planes. Therefore, the surface-based comparison assessed in terms of both point-to-plane error magnitude and the geometric orientation consistency of the reconstructed wall panels. It should be noted that selecting five representative photogrammetric model points may limit the stability of the fitted planes, specifically in weakly reconstructed regions. Therefore, the surface-based results should be interpreted as a representative planar-surface comparison rather than a full dense point cloud segmentation analysis. This limitation is particularly relevant for the nadir model, where some upper-floor and under-eave surfaces could not provide enough reliable points for plane fitting.

ISSN: 1686-6576 (Printed) | ISSN 2673-0014 (Online) | © Geoinformatics International

2.8 Statistical Analysis

All the mentioned differences obtained in the study were evaluated using both descriptive statistics and appropriate significance tests. Main approach involves basic quality metrics such as mean signed error, mean absolute error (MAE), RMSE, standard deviation, and maximum absolute error. In the point-based comparisons, these metrics were determined separately for the three coordinate axes as well as for the 2D and 3D error components. In the length-based comparisons, the same error metrics were calculated based on the differences between the reference and hybrid model values. Also, in the surface-based comparisons, the deviations of the photogrammetric surface points from the reference plane and the angular differences between the normal vectors were computed respectively.

Distributional characteristics of the residuals were first examined statistically by using the Shapiro–Wilk test. According to the normal distribution of these values, parametric (Paired T-test) or non-parametric (Wilcoxon signed-rank) tests were used to assess both mean error magnitudes and statistical significance of the observed differences. This approach enabled a more reliable interpretation of the effects of different data acquisition strategies on building-based photogrammetric performance [45][46] and [47]. The Shapiro–Wilk test was used as a diagnostic tool to examine the distributional characteristics of the residuals in this study. However, it should be noted that the sample sizes in some comparisons were relatively small, particularly for the common point- and the length-based comparison. Therefore, this test may have limited statistical power to detect departures from normality and was not used as the only basis for interpretation, and both parametric and non-parametric paired test results were considered for the main paired comparisons. The paired t-test was used to evaluate mean differences under the assumption of normality, while the Wilcoxon signed-rank test was used as a distribution-free alternative. When both tests led to the same interpretation, the result was considered more robust. If the two tests differed, the Wilcoxon signed-rank result was interpreted more cautiously because of the small sample size and possible non-normality of the residuals. The statistical findings were evaluated together with descriptive error metrics.

Because several paired statistical tests were performed simultaneously in the common-point comparison, a Bonferroni correction was applied to control the error rate, and the corrected significance level was calculated as $\alpha = 0.05 / 5 = 0.01$. Therefore, the statistical results were interpreted also including Bonferroni-corrected threshold. This correction was used to determine whether the observed differences remained statistically significant after accounting for multiple testing.

3. Results and Discussion

3.1 Point-based comparison results

The point-based performance of the photogrammetric models was evaluated for the comparison. For this purpose, the extent to which the reference points could be reconstructed in each model was examined (Table 6). The point-based comparison indicates that the main difference between the two photogrammetric models is related to coordinate accuracy and feature availability. The nadir model could not provide reliable positions for several façade details, particularly in upper-floor and under-eave regions. This pattern is expected because nadir image blocks observe vertical façade elements with weak intersection geometry, limited incidence-angle diversity, and sparse tie point density. In contrast, the hybrid model enables increase in the number of interpretable façade details by adding oblique and façade-oriented images (Table 7). The 60% comparability rate of the nadir model should be interpreted as a direct indicator of limited feature availability rather than missing data ratio. In contrast, all of these points could be identified in the hybrid model because the additional oblique and façade-oriented images improved the visibility and geometric definition of the corresponding façade details. This finding supports the idea that viewing geometry is a critical factor in building-scale UAV photogrammetry, especially when the target features are located on vertical façades instead of horizontal roof or ground surfaces. In order to evaluate both models, error statistics with respect to the 3-coordinate axis were executed (Table 8).

Table 6: Matching and computation status of the reference point coordinates in the photogrammetric models

Model	Total Number of Reference Points	Number of Comparable Points	Number of non-Represented Points	Comparability Rate (%)
Nadir	35	21	14	60
Hybrid	35	35	0	100

ISSN: 1686-6576 (Printed) | ISSN 2673-0014 (Online) | © Geoinformatics International

Table 7: Reference points that cannot be represented in the nadir-only model and non-comparability reasons

Point Group	Point IDs	Interpretation
Non-presented points in the nadir-only model	5, 8, 11, 13, 15, 17, 19, 20, 25, 27, 29, 31, 33, 34	Points not reliably identified in the nadir model
Main photogrammetric reason	-	Weak nadir viewing geometry on vertical façades, sparse tie points, local point cloud noise, occlusion around upper-floor and under-eave regions
Effect on analysis	-	Points excluded from nadir error statistics but available in the hybrid model

Table 8: Axis-based error statistics. The results are based on the coordinate differences between the reference measurements and the nadir and hybrid models

Model Type	Coordinate Axis	Number of Points	Mean Signed Error (m)	MAE (m)	RMSE (m)	Standard Deviation (m)	Max. Absolute Error (m)
Nadir	ΔY	21	-0.022	0.025	0.027	0.015	0.052
Nadir	ΔX	21	0.023	0.030	0.039	0.032	0.099
Nadir	ΔZ	21	0.355	0.355	0.452	0.286	1.141
Hybrid	ΔY	35	-0.017	0.019	0.023	0.016	0.060
Hybrid	ΔX	35	0.005	0.015	0.018	0.017	0.038
Hybrid	ΔZ	35	-0.021	0.029	0.035	0.029	0.093

The axis-based results indicate that the vertical component is the most vulnerable part of the nadir-only workflow. This behavior can be explained by the weak intersection geometry of nadir images on vertical wall surfaces. Although RTK-supported camera positions improve direct georeferencing, they cannot fully compensate for weak ray convergence when façade details are not sufficiently observed from multiple directions. As a result, errors in the nadir model are concentrated mainly in the vertical component rather than being uniformly distributed across all coordinate axes. The hybrid image set reduced this weakness by increasing the diversity of viewing directions and by improving the visibility of window surroundings, façade details, and under-eave regions. Thus, the vertical improvement observed in the hybrid model should be interpreted as a geometric effect of the acquisition strategy.

On the other hand, large vertical RMSE observed in the nadir model should not be interpreted as a general RTK positioning failure or as an instability of the photogrammetric block. The processing quality metrics in the previous table demonstrate low reprojection errors, complete image calibration, and cm-level geolocation residuals for both models. Hence, the main source of the large Z-axis error for the nadir model is interpreted as a local façade reconstruction and point-identification problem rather than a global processing failure. The same model was not able to reconstruct a clear definition for physical corner points which are located near to the upper floor. Because nadir imagery observes vertical wall surfaces with weak incidence-angle diversity and limited ray convergence, the dense point cloud in these regions may be sparse, noisy, vertically smeared, or displaced toward adjacent roof/eave surfaces. As a result, the manually identified model point may not correspond exactly to the same physical detail measured by the terrestrial observations, even when the surrounding façade region is visually represented in the model. This mismatch between the reference and the nearest interpretable nadir-derived point can produce large vertical residuals. Thus, the high Z-axis RMSE reflects the practical failure of the nadir-only model to reproduce façade detail points under weak viewing geometry, rather than a failure of RTK direct georeferencing alone.

To evaluate the effect of point-based accuracy on overall positioning performance, the error magnitudes in the horizontal position and three-dimensional coordinates were also examined separately (Table 9). According to Table 9, horizontal and 3D positional error metrics demonstrate that the nadir model error is largely caused by the vertical component. This is important for building documentation because façade elements are often used as endpoints of linear and surface-based measurements. This vertical uncertainty in individual points may affect the practical measurements of certain features on planar walls. To determine whether the improvement was caused only by the larger number of points in the hybrid model, an additional common-point comparison was conducted using only the points reconstructed in both models (Table 10). This situation is also supported by the 3D error behavior, because the overall 3D error in the nadir model is strongly influenced by the vertical component. In practice, the nadir model may still provide usable horizontal positions for some visible façade details but becomes unreliable when the same points are required for height-sensitive tasks such as vertical façade measurements, window-corner extraction, or surface-plane construction.

Since five simultaneous paired comparisons were performed for the common points in both models, a Bonferroni correction was applied to control the family-wise error rate. The corrected significance threshold was calculated as ($\alpha = 0.05 / 5 = 0.01$), and the ΔZ MAE, horizontal RMSE, and 3D RMSE differences remained statistically significant according to this corrected value. The ΔY MAE difference was not statistically significant, and for ΔX MAE, the Wilcoxon signed-rank test indicated statistical significance after Bonferroni correction, whereas the paired t-test p value was slightly above the corrected threshold. Therefore, the ΔX result was interpreted cautiously. Overall, the Bonferroni correction did not change the main conclusion of the common-point analysis: the hybrid model provided a clear improvement, particularly in the vertical and overall 3D accuracy components. This supports the interpretation that the additional oblique and façade-oriented images improved the geometric reliability of façade point reconstruction.

3.2 Length-based Comparison Results

The length-based evaluation was used to find out whether the observed point-level differences affected practical linear measurements or not. This comparison requires both endpoints of a selected linear element to be reliably identified on the photogrammetric models. Such difficulties may arise if one or both endpoints could not be interpreted clearly or observed, and this revised analysis included the nadir model as well wherever this condition was met (Table 11). The length-based comparison provides a complementary interpretation of the point-based results. The nadir model could provide length measurements only for a limited number of points around the lower-floor window edges, where both endpoints were clearly visible.

Table 9: 2D and 3D error magnitudes of both photogrammetric models with respect to the reference points

Metric	Nadir Model	Hybrid Model
Number of Points	21	35
Mean Horizontal Error (m)	0.041	0.025
Horizontal MAE (m)	0.041	0.025
Horizontal RMSE (m)	0.047	0.029
Horizontal Standard Deviation (m)	0.024	0.015
Max. Horizontal Error (m)	0.104	0.071
Mean 3D Error (m)	0.359	0.042
3D MAE (m)	0.359	0.042
3D RMSE (m)	0.454	0.046
3D Standard Deviation (m)	0.285	0.018
Max. 3D Error (m)	1.146	0.117

Table 10: Statistical comparison of the common observed points reconstructed in nadir and hybrid models with Bonferroni correction

Error Metrics	No. of common points	Nadir model (m)	Hybrid model (m)	Improvement (%)	Paired t-test p value	Wilcoxon test P value	Bonferroni threshold
Δ*X* MAE	21	0.03	0.013	56.7	0.01	0.01	0.01
Δ*Y* MAE	21	0.025	0.020	21.2	0.17	0.10	0.01
ΔZ MAE	21	0.355	0.025	92.9	<0.0001	<0.0001	0.01
Horizontal RMSE	21	0.047	0.028	39.9	0.01	0.01	0.01
3D RMSE	21	0.454	0.041	91.0	<0.0001	<0.0001	0.01

ISSN: 1686-6576 (Printed) | ISSN 2673-0014 (Online) | © Geoinformatics International

Table 11: Length-based comparison of reference, nadir, and hybrid model-derived measurements. Lengths that cannot be computed from the model as marked as Not Computed (NC)

Length No	Reference Length (m)	Nadir Length (m)	Nadir Residual (m)	Nadir Absolute Residual (m)	Hybrid Length (m)	Hybrid Residual (m)	Hybrid Absolute Difference (m)
1	3.239	NC	NC	NC	3.273	-0.034	0.034
2	3.218	NC	NC	NC	3.257	-0.039	0.039
3	3.238	NC	NC	NC	3.228	0.01	0.01
4	3.253	NC	NC	NC	3.257	-0.004	0.004
5	1.941	NC	NC	NC	1.947	-0.006	0.006
6	1.945	1.950	-0.005	0.005	1.944	0.001	0.001
7	1.954	NC	NC	NC	1.961	-0.007	0.007
8	1.907	1.910	-0.003	0.003	1.895	0.012	0.012
9	3.261	NC	NC	NC	3.271	-0.01	0.01
10	1.958	NC	NC	NC	1.947	0.011	0.011
11	1.923	1.910	0.013	0.013	1.919	0.004	0.004
12	1.92	NC	NC	NC	1.914	0.006	0.006
13	1.916	1.910	0.006	0.006	1.904	0.012	0.012
14	3.235	NC	NC	NC	3.229	0.006	0.006

This indicates that nadir imagery can produce acceptable length estimates under favorable visibility conditions, but its practical usability decreases when façade endpoints are located on the upper-floor or under-eave regions. In contrast, the hybrid model allowed all selected length pairs to be evaluated. Therefore, the main advantage of the hybrid model in the length-based analysis should not be interpreted as uniformly lower error for all common elements. For the four length pairs that could be measured in both models, the nadir and hybrid errors were similar. However, the nadir model was limited to these clearly visible lower-floor window edges, whereas the hybrid model enabled all 14 selected length pairs to be evaluated. Thus, the empirical advantage of the hybrid workflow is its substantial higher measurement completeness and practical usability, rather than a uniform reduction in length error for the limited subset visible in both models.

The larger residuals observed for lengths 1 and 2 should be interpreted more carefully because their magnitudes exceed the expected uncertainty of the terrestrial reference measurements. The reflectorless total station measurements used as reference data have mm-level distance precision; therefore, these 34 mm and 39 mm differences cannot be attributed to the reference measurement uncertainty alone and are more likely related to the photogrammetric identification of the corresponding endpoints in the hybrid model. These lengths were derived from façade features whose endpoints were more sensitive to local point cloud quality and manual point identification. Around window corners and façade edges, the photogrammetric point cloud may contain locally noisy or mixed points because of weak surface texture, edge discontinuities, partial occlusion, and the transition between wall, window frame, and under-eave elements. Since no automatic snapping was applied, the points for these length measurements were manually selected from the dense point cloud and image-supported model view. Therefore, small point shifts at one or both ends of a line could propagate directly into the final length residual. For this reason, the larger errors for lengths 1 and 2 were interpreted as local endpoint-definition errors in the photogrammetric model rather than as errors in the terrestrial reference measurements. Despite these larger residuals, the remaining length comparisons indicate that the hybrid model generally provided usable linear measurements. However, these results also show that length-based accuracy is strongly dependent on the clarity and repeatability of endpoint identification, particularly for façade details located near edges, windows, and occlusion-sensitive regions (Table 12).

Table 12: Statistics for the length-based comparison

Model	Number of lengths	Computable lengths	Not computable lengths	Computability rate (%)	Mean signed residual (m)	MAE (m)	RMSE (m)
Nadir	14	4	10	28.6	0.003	0.007	0.008
Hybrid	14	14	0	100.0	-0.003	0.012	0.016

Table 13: Summary statistics of the length-based comparison

Comparison	n	Shapiro-Wilk p value	Paired T-test p value	Wilcoxon p value
Nadir-reference (for measured 4 lengths)	4	0.54	0.56	0.63
Hybrid-reference (14 lengths)	14	0.01	0.54	0.95
Hybrid-reference (common 4 lengths)	4	0.18	0.08	0.13

The length-based comparison indicates that the nadir model allowed only 4 of the 14 selected length pairs to be measured, corresponding to a computability rate of 28.6%, and were all located on lower-floor window edges, where the façade details were more clearly visible in the nadir-derived model. Other remaining measurements could not be calculated from the nadir model because at least one endpoint of each pair could not be identified due to missing geometry, occlusion, or noisy reconstruction. For the four common length pairs, the nadir and hybrid models produced similar error magnitudes. This indicates that nadir imagery can provide acceptable length estimates only for clearly visible lower-floor details. However, the hybrid model enabled all 14 selected length pairs to be measured. Therefore, the main advantage of the hybrid model in the length-based evaluation is the measurement capability and practical detection, rather than uniformly lower errors for the limited set of features visible in both models (Table 13).

The length-based results should also be interpreted in relation to point identification uncertainty. Since the lengths were calculated from manually selected photogrammetric model points, the reliability of each length depends on whether both endpoint features were clearly visible and geometrically well defined in the model. This explains why the nadir model could provide only a limited number of length measurements, whereas the hybrid model provided a more complete set of measurable linear elements. Because of the small sample size in the length-based comparison, the Wilcoxon signed-rank result was interpreted cautiously. The high Wilcoxon p value does not necessarily indicate that the photogrammetric and terrestrial lengths are identical, and there was no statistically significant evidence of a systematically signed difference within this limited sample. The residual signs were also relatively balanced, with both positive and negative residuals. In addition, the two largest residuals, observed for lengths 1 and 2 were examined to determine whether they affected the statistical interpretation, and an additional sensitivity check was performed by excluding these values. The results indicated that the MAE and RMSE decreased to 0.007 m and 0.008 m respectively, and the statistical tests still did not indicate a significant systematic difference between the reference and hybrid-derived lengths. Therefore, the large residuals of lengths 1 and 2 were interpreted as local endpoint-definition errors rather than evidence of a systematic scale or length bias in the hybrid model. Nevertheless, because of the small number of length observations, the statistical result should be interpreted together with the descriptive error metrics and the point visibility conditions.

In addition, the Wilcoxon signed-rank test was computed using the two-sided test with the automatic method selection. For the 14 hybrid length residuals, repeated absolute residual values were present; therefore, the reported p value may slightly differ depending on the exact or approximate Wilcoxon calculation method. The statistical interpretation remains unchanged in either case. To provide a more informative assessment of possible systematic bias, a 95% confidence interval was calculated for the mean signed residual of the hybrid-derived lengths, and the mean signed residual was computed as -0.0027 m, with a 95% confidence interval from -0.0120 m to 0.0066 m. This indicates that the average systematic length bias was close to zero and remained within approximately cm-level for this dataset. A sensitivity check was also performed by excluding lengths 1 and 2, which had the largest residuals. After excluding these two lengths, the mean signed residual became 0.003 m, and the 95% confidence interval narrowed to -0.002 m to 0.008 m. This confirms that lengths 1 and 2 affected the residual dispersion, but they did not indicate a consistent systematic length bias. Therefore, the length-based results were interpreted together with descriptive error metrics, point visibility conditions, and confidence interval, rather than relying only on the Wilcoxon p value alone.

The statistical test results should be interpreted together with the limited number of common length pairs, and the absence of a statistically significant does not indicate equivalent overall performance between the two models. Instead, this situation demonstrates that both models can provide comparable length measurements only when the selected features are clearly visible and reliably identifiable. The practical advantage of the hybrid model is that it expands this capability to all selected length pairs, whereas the nadir model remains limited to a small subset for lower-floor features.

3.3 Surface-based Comparison Results

For the surface-based assessment, seven virtual planar surfaces with different spatial distributions on the building were selected (Table 14). These surfaces were defined to represent the lower and upper floors on the building façades, and the approximate dimensions and number of reference points were determined for each surface. The surface-based comparison indicates that surface representation is strongly controlled by visibility and viewing geometry. The surfaces that could not be evaluated in the nadir model were located in upper-floor or under-eave regions, where nadir imagery provided weak geometric support. This confirms that a surface may not be suitable for evaluation even if the building is generally reconstructed in a classical photogrammetric model. The hybrid workflow improved surface availability by adding additional viewing directions toward the façade and eave-affected wall panels. This finding demonstrates that the hybrid approach provides greater coverage in terms of surface representation (Figure 6). Figure 6 visually supports the surface-based findings by showing that the nadir model produced insufficient point cloud representation beneath the eaves. This visual evidence is important because the limitation is a numerical accuracy issue in addition to a reconstruction completeness problem. In such regions, the absence of a continuous and interpretable surface patch prevents reliable plane fitting and subsequent surface comparison. For this surface, the hybrid model yielded slightly lower MAE and RMSE values than the nadir model which indicates a small improvement in average residual magnitude. However, the nadir residuals were more uniformly distributed and showed a lower standard deviation, whereas the hybrid residuals exhibited a wider spread, including both negative and positive values. The maximum absolute residuals of the two models were nearly identical. Therefore, this example surface suggests that the hybrid model may provide a slight improvement in average geometric agreement for some comparable surfaces, but it does not necessarily produce a more uniform local residual pattern in every case (Table 15). The comparison between reference and photogrammetric surfaces is presented in Table 15, and results should be interpreted by considering both error magnitude and surface availability. The nadir model produced lower errors on some of the surfaces that could be evaluated, but these surfaces represent only on more visible parts of the façades. The hybrid model, on the other hand, included more difficult upper-floor and under-eave surfaces (Table 16). Therefore, slightly higher local errors in the hybrid model do not necessarily indicate poorer practical performance; but the hybrid model was evaluated on a more complete and more challenging set of surfaces.

Table 14: Specifications of the planar surfaces for surface-based comparison

Surface No	Façade	Surface Type	Approx. Dimensions	Number of Reference Points	Surface Reconstruction in the Nadir Model	Surface Reconstruction in the Hybrid Model
1	East-Lower floor	Flat wall surface	3 m x 1.7 m	12	Reconstructed	Reconstructed
2	North-Upper floor	Flat wall surface	2 m x 1.5 m	10	Not reconstructed	Reconstructed
3	North-Lower floor	Flat wall surface	2 m x 1.5 m	9	Reconstructed	Reconstructed
4	North-Lower floor	Flat wall surface	2 m x 1.5 m	9	Reconstructed	Reconstructed
5	North-Upper floor	Flat wall surface	2 m x 1.5 m	9	Not reconstructed	Reconstructed
6	West-Lower floor	Flat wall surface	2.8 m x 1.5 m	9	Reconstructed	Reconstructed
7	West-Upper floor	Flat wall surface	3 m x 1.5 m	12	Not reconstructed	Reconstructed

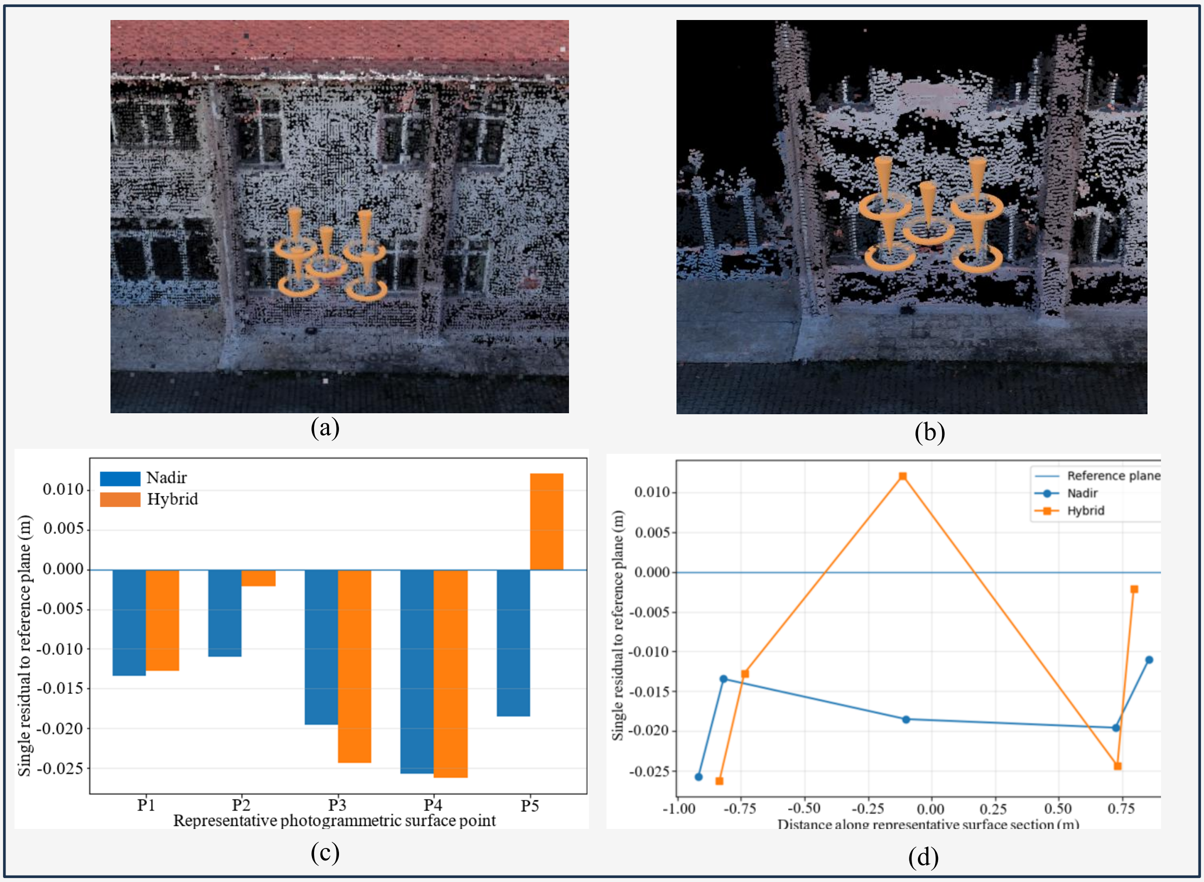

Figure 6. Representative surface-based comparison for Surface 3: (a) and (b) show the selected wall surface in the hybrid and nadir photogrammetric models with brown points, respectively. (c) presents the signed point-to-plane residuals of the representative photogrammetric surface points with respect to the terrestrial reference plane, and (d) shows the cross-sectional residual profile of the same surface along the dominant in-plane direction. The figure illustrates that the hybrid model provided slightly lower average residual magnitudes for this representative surface, while the nadir model showed a more uniform residual distribution

Table 15: Quality and error metrics for the surfaces reconstructed with the terrestrial observations

Surface No	Mean Signed Deviation (m)	Mean Absolute Deviation (m)	RMSE (m)	Standard Deviation (m)	Max. Absolute Deviation (m)
1	0.000	0.002	0.003	0.003	0.007
2	0.000	0.002	0.003	0.003	0.004
3	0.000	0.002	0.003	0.003	0.005
4	0.000	0.003	0.003	0.003	0.006
5	0.000	0.003	0.003	0.004	0.005
6	0.000	0.002	0.002	0.002	0.006
7	0.000	0.002	0.002	0.002	0.004

Table 16: Comparison of reference and photogrammetric model derived surfaces

Surface No	Model Type	Number of Photogram-metric Points	Mean Signed Deviation (m)	Mean Absolute Deviation (m)	RMSE (m)	SD (m)	Max. Absolute Deviation (m)	Angle Between Normal Vectors (°)
1	Nadir	5	0.006	0.036	0.042	0.046	0.076	0.186
	Hybrid	5	0.048	0.048	0.052	0.023	0.075	0.943
2	Nadir	-	-	-	-	-	-	-
	Hybrid	5	-0.082	0.082	0.096	0.057	0.160	3.967
3	Nadir	5	-0.018	0.018	0.018	0.006	0.026	0.556
	Hybrid	5	-0.011	0.016	0.018	0.016	0.026	1.125
4	Nadir	5	0.008	0.018	0.020	0.020	0.028	1.896
	Hybrid	5	-0.033	0.037	0.054	0.048	0.097	4.320
5	Nadir	-	-	-	-	-	-	-
	Hybrid	5	0.049	0.049	0.057	0.032	0.105	0.496
6	Nadir	5	0.036	0.054	0.070	0.067	0.133	4.413
	Hybrid	5	-0.009	0.033	0.037	0.040	0.056	2.801
7	Nadir	-	-	-	-	-	-	-
	Hybrid	5	-0.051	0.055	0.065	0.044	0.106	1.073

The surface-based results should be interpreted with caution because the hybrid model did not provide lower error magnitudes for every surface. For the common regions, the nadir model produced lower RMSE values for Surfaces 1 and 4, whereas the hybrid model produced lower RMSE values for Surfaces 3 and 6. Therefore, the surface-based comparison does not support a general conclusion that the hybrid model is uniformly more accurate than the nadir model in terms of local surface RMSE. The lower RMSE values obtained from the nadir model on Surfaces 1 and 4 can be explained by the local characteristics of these surfaces, which are located in lower-floor or more clearly visible façade regions, and the nadir image block could still provide sufficient surface representation. In such observable regions, the nadir-only model may benefit from a simpler and more homogeneous image block geometry and a smaller average GSD. On the other hand, the hybrid dataset combines multiple oriented images with different viewing directions and a larger average GSD. Although this geometry improves the visibility and reconstruction of upper-floor and under-eave regions, it may also introduce more local point dispersion or slight surface offsets on visible wall panels.

To further examine the orientation consistency of the reconstructed surfaces, the normal-vector angle differences were compared for the four surfaces that were reconstructed in both models. For these common surfaces, the angle differences between the hybrid and nadir models were 0.757°, 0.569°, 2.424°, and -1.612° for Surfaces 1, 3, 4, and 6, respectively. The mean difference was 0.535° and the median difference was 0.6631°, indicating that the hybrid model had larger normal-vector angle differences for three of the four common surfaces. However, statistical tests did not indicate that the hybrid model normals were significantly worse than those of the nadir model. The paired t-test yielded $p = 0.5646$, and the Wilcoxon signed-rank test yielded $p = 0.6250$. Therefore, the observed increase in normal-vector angle differences for some common surfaces should be interpreted as a descriptive tendency rather than a statistically significant degradation. These findings indicate that the hybrid workflow should not be interpreted as providing uniformly stronger surface orientation accuracy. The stronger geometric configuration of the hybrid image block mainly improved façade visibility, surface availability, and the ability to reconstruct upper-floor and under-eave regions. However, for surfaces already visible in the nadir model, the hybrid model may produce larger local angular deviations because of mixed viewing directions, larger average GSD, manual façade-oriented image integration, and local point-cloud dispersion. Thus, the surface-based results indicate a trade-off between surface completeness and local orientation consistency.

In addition, the advantage of the hybrid model should not be interpreted as a uniform reduction in surface error metrics. Instead, its main contribution in the surface-based comparison is its ability to reconstruct and evaluate all selected surfaces,

ISSN: 1686-6576 (Printed) | ISSN 2673-0014 (Online) | © Geoinformatics International

including those that were not measurable in the nadir model. For engineering tasks focused only on a small number of clearly visible surfaces, the nadir model may provide equal or lower local surface errors. However, for applications requiring complete façade documentation, upper-floor inspection, and under-eave surface representation, the hybrid model provides greater practical usability despite higher local errors on some reconstructed surfaces. Therefore, the selection between nadir-only and hybrid acquisition should be based on the intended engineering task. The proposed hybrid workflow is more appropriate when completeness, measurability, and coverage of occlusion-sensitive façade regions are required. In this study, the hybrid model was considered more useful for building documentation because the objective was not only to minimize local surface errors, but also to evaluate whether all selected façade surfaces could be represented and measured (Figure 7).

When the point-, length-, and surface-based results are considered together, the results indicate that a single accuracy metric is not sufficient for evaluating building-scale UAV photogrammetric models. The nadir model may provide acceptable results for clearly visible and geometrically observable façade details, but it is limited in terms of feature availability, measurement completeness, and surface representation. On the other hand, the hybrid model improves practical measurability by increasing viewing-angle diversity and reducing visibility gaps in vertical and under-eave regions. Thus, the main contribution of the hybrid workflow is not a uniform reduction for all error metrics, but a more complete and practically usable geometric representation of façade details, specifically in regions where nadir imagery has limited visibility. This is an important outcome for building documentation workflows, where the availability of measurable information is often as critical as the magnitude of local geometric error.

To provide an unbiased comparison between the two photogrammetric models, a separate common-surface-only analysis was also performed using only the surfaces that were reconstructed in both models for the surfaces 1, 3, 4, and 6. This analysis was conducted separately from the surface-completeness assessment in order to compare the local error metrics under equivalent surface availability conditions (Table 17). According to Table 17, the comparison indicates that the hybrid model did not provide a statistically significant reduction in local surface error metrics for the surfaces reconstructed in both models. The nadir model produced slightly lower mean MAE and RMSE values, whereas the hybrid model produced slightly lower mean standard deviation and maximum absolute deviation values. The hybrid model also had a larger normal-vector angle difference.

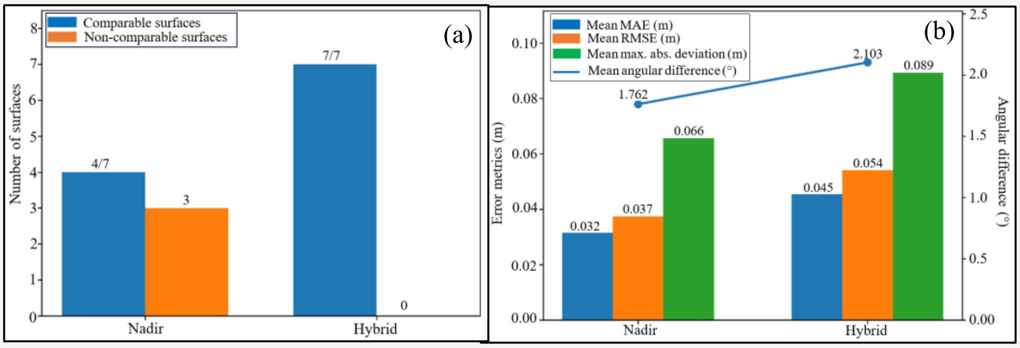

Figure 7: Overall surface representation performance of the nadir and hybrid photogrammetric models. Panel (a) shows the number of comparable and non-comparable reference surfaces, while panel (b) summarizes the mean surface error metrics and the mean angular difference between reference and photogrammetric surfaces

Table 17: Surface-based error metrics for the common wall panels

Metric	n	Nadir mean	Hybrid mean	Hybrid-Nadir mean	Hybrid-Nadir median	Shapiro-Wilk p value	Paired T-test p value	Wilcoxon p value
Mean signed deviation (m)	4	0.008	-0.001	-0.009	-0.017	0.38	0.69	0.88
MAE (m)	4	0.031	0.033	0.002	0.005	0.74	0.84	1.00
RMSE (m)	4	0.037	0.040	0.003	0.005	0.94	0.85	0.88
Standard deviation (m)	4	0.035	0.032	-0.003	-0.007	0.33	0.82	1.00
Max. abs. deviation (m)	4	0.066	0.064	-0.002	-0.000	0.71	0.95	0.88
Normal angle (°)	4	1.762	2.297	0.535	0.663	0.76	0.57	0.63

ISSN: 1686-6576 (Printed) | ISSN 2673-0014 (Online) | © Geoinformatics International

However, none of these differences were statistically significant according to either the Paired T-test or the Wilcoxon signed-rank test. The results in this study should not be interpreted as a universal superiority of the hybrid model in all accuracy criteria, but the two acquisition strategies serve different priorities. The nadir-only model may be sufficient or even preferable when the target surfaces are visible from above and the main requirement is local precision on a limited number of panels. The hybrid model becomes advantageous when the task requires a more complete and interpretable representation of façade surfaces, especially in upper-floor and under-eave regions. This distinction is important because engineering applications may prioritize precision, completeness, processing simplicity, field efficiency, or documentation coverage differently.

4. Conclusion

In this study, nadir-only and hybrid RTK-UAV photogrammetric workflows for building surface detail extraction were evaluated against independent terrestrial reference measurements. The comparison in this manner was carried out at three complementary levels: point-based coordinate accuracy, length-based measurement performance, and surface-based planar representation. The results indicate that the performance of UAV-derived building models cannot be adequately assessed using a single accuracy metric. Feature availability, measurement completeness, local geometric accuracy, and surface-orientation consistency must be interpreted together when selecting an image acquisition strategy for façade documentation.

The strongest improvement obtained from the hybrid workflow was observed in point-based comparison. The hybrid model enabled all reference façade points to be measured and substantially reduced the vertical and overall 3D coordinate errors compared with the nadir-only model. This result indicates that additional oblique and façade-oriented images can improve the reconstruction of façade details that are weakly represented in nadir-only imagery, specifically in upper-floor and under-eave regions. However, this point-based improvement should not be generalized to all accuracy criteria without qualification. Second, the length-based results indicate that the hybrid model provided practically usable measurements for the selected façade elements. The nadir model could be included only where both endpoints of a selected linear element were clearly observable, whereas the hybrid model allowed all selected length pairs to be evaluated. Therefore, the main contribution of the hybrid workflow is related to measurement availability and practical measurability in this manner. The results do not imply that the hybrid workflow is always necessary for every linear measurement task, especially when the target endpoints are clearly visible and reliably identifiable in nadir imagery.

On the other hand, the surface-based results show a more complex trade-off. The hybrid model enabled all selected surfaces to be evaluated, including upper-floor and under-eave wall panels that were not reconstructed in the nadir model. However, the common-surface analysis indicates that the hybrid model did not provide a statistically significant reduction in local surface error metrics for the surfaces reconstructed in both models. In addition, the hybrid model showed larger normal-vector angle differences on several common surfaces. Although these differences were not statistically significant, the hybrid workflow should not be interpreted as uniformly superior in terms of local RMSE or surface-orientation accuracy. The main advantage is the improved surface completeness and practical measurability, rather than a consistent reduction in all surface error metrics.

From a practical perspective, nadir-only acquisition may be sufficient in some cases when the objective is limited to roofs, open areas, clearly visible lower façade panels, single-story structures, or façades without significant eave overhangs or occlusion. This approach may also be preferable when the primary target is local precision on a small number of surfaces and field efficiency, simple acquisition, and processing simplicity are more important than complete façade coverage. In contrast, the hybrid workflow becomes more useful when the task requires upper-floor façade documentation, under-eave inspection, window-surrounding detail extraction, or complete surface representation in areas where nadir imagery has limited visibility. Thus, the selection between nadir-only and hybrid acquisition should depend on the intended engineering task rather than on the general assumption that one model is always more accurate than the other.

Several limitations should be considered when interpreting the results. The experiment was conducted on a single two-story educational building with a specific U-shaped plan, façade texture, eave geometry, and courtyard environment. Therefore, the findings may not be directly transferable to buildings with different heights, façade materials, occlusion conditions, or architectural complexity. Also, the models were processed using RTK-supported direct georeferencing without GCPs in the bundle adjustment. Although independent terrestrial measurements were used for validation, the results should not be interpreted as representing GCPconstrained photogrammetric workflows. In addition, the uncertainty contributions from GNSS positioning, reflectorless total station observations, RTK image positions, manual point selection, endpoint identification, and plane fitting were not propagated into a combined uncertainty model, and the acquisition-density effect was not isolated as an independent variable, because the nadir and hybrid datasets differed in viewing geometry, image number, GSD, and manual façade-image distribution. Finally, the manual component of the hybrid workflow introduces operator dependency and may increase field effort, flight-planning complexity, processing workload, and reproducibility limitations compared with a fully autonomous nadir-only workflow.

Overall, the results support the use of hybrid RTK-UAV acquisition for building documentation tasks where completeness, measurability, and visibility of occlusion-sensitive façade regions are critical. However, the hybrid workflow should be regarded as a task-dependent strategy rather than a universally more accurate solution. For well-visible surfaces and simple building geometries, nadir-only acquisition may provide adequate or even lower local surface errors with a simpler workflow. For complex façades, upper-floor regions, and under-eave surfaces, hybrid acquisition provides a more complete and practically usable representation, but its local surface accuracy and surface-orientation consistency should still be verified using independent reference measurements.

References

[1] Lee, E., Park, S., Jang, H., Choi, W. and Sohn, H. G., (2024). Enhancement of Low-Cost UAV-based Photogrammetric Point Cloud Using MMS Point Cloud and Oblique Images for 3D Urban Reconstruction. *Measurement,* Vol. 226. https://doi.org/10.1016/j.measurement.2024.114158.

[2] Chiabrando, F., Nex, F., Piatti, D. and Rinaudo, F., (2011). UAV and RPV Systems for Photogrammetric Surveys in Archaeological Areas: Two Tests in the Piedmont Region (Italy). *Journal of Archaeological Science,* Vol. 38(3), 697-710. https://doi.org/10.1016/j.jas.2010.10.022.

[3] Remondino, F., Barazzetti, L., Nex, F., Scaioni, M. and Sarazzi, D., (2011). UAV Photogrammetry for Mapping and 3D Modeling - Current Status and Future Perspectives. International Archives of the Photogrammetry, Remote Sensing and Spatial Information Sciences, Vol. XXXVIII-1/C22, 25-31. https://doi.org/10.5194/isprsarchives-XXXVIII-1-C22-25-2011.

[4] Colomina, I. and Molina, P., (2014). Unmanned Aerial Systems for Photogrammetry and Remote Sensing: A Review. *ISPRS Journal of Photogrammetry and Remote Sensing,* Vol. 92, 79-97. https://doi.org/10.1016/j.isprsjprs.2014.02.013.

[5] Harwin, S. and Lucieer, A., (2012). Assessing the Accuracy of Georeferenced Point Clouds Produced via Multi-View Stereopsis from Unmanned Aerial Vehicle (UAV) Imagery. *Remote Sensing,* Vol. 4, 1573-1599. https://doi.org/10.3390/rs4061573.

[6] Elkhrachy, I., (2021). Accuracy Assessment of Low-Cost Unmanned Aerial Vehicle (UAV) Photogrammetry. *Alexandria Engineering Journal,* Vol. 60(6), 5579-5590. https://doi.org/10.1016/j.aej.2021.04.011.

[7] Agüera-Vega, F., Carvajal-Ramírez, F. and Martínez-Carricondo, P., (2017). Assessment of Photogrammetric Mapping Accuracy Based on Variation Ground Control Points Number using Unmanned Aerial Vehicle. *Measurement,* Vol. 98, 221-227. https://doi.org/10.1016/j.measurement.2016.12.002.

[8] Sanz-Ablanedo, E., Chandler, J. H., Rodríguez-Pérez, J. R. and Ordóñez, C., (2018). Accuracy of Unmanned Aerial Vehicle (UAV) and SfM Photogrammetry Survey as a Function of the Number and Location of Ground Control Points Used. *Remote Sensing,* Vol. 10. https://doi.org/10.3390/rs10101606.

[9] James, M. R., Robson, S., d'Oleire-Oltmanns, S. and Niethammer, U., (2017). Optimising UAV Topographic Surveys Processed with Structure-From-Motion: Ground Control Quality, Quantity and Bundle Adjustment. *Geomorphology,* Vol. 280, 51-66. https://doi.org/10.1016/j.geomorph.2016.11.021.

[10] Furby, B. and Akhavian, R., (2024). A Comprehensive Comparison of Photogrammetric and RTK-GPS Methods for General Order Land Surveying. *Buildings,* Vol. 14. https://doi.org/10.3390/buildings14061863.

[11] Benassi, F., Dall’Asta, E., Diotri, F., Forlani, G., Morra di Cella, U., Roncella, R. and Santise, M., (2017). Testing Accuracy and Repeatability of UAV Blocks Oriented with GNSS-Supported Aerial Triangulation. *Remote Sensing,* Vol. 9. https://doi.org/10.3390/rs9020172.

[12] Ekaso, D., Nex, F. and Kerle, N., (2020). Accuracy Assessment of Real-Time Kinematics (RTK) Measurements on Unmanned Aerial Vehicles (UAV) for Direct

Geo-Referencing. *Geo-spatial Information Science,* Vol. 23(2), 165-181. https://doi.org/10.1080/10095020.2019.1710437.

[13] Štroner, M., Urban, R., Reindl, T., Seidl, J. and Brouček, J., (2020). Evaluation of the Georeferencing Accuracy of a Photogrammetric Model Using a Quadrocopter with Onboard GNSS RTK. *Sensors,* Vol. 20. https://doi.org/10.3390/s20082318.

[14] Martínez-Carricondo, P., Agüera-Vega, F. and Carvajal-Ramírez, F., (2023). Accuracy Assessment of RTK/PPK UAV-Photogrammetry Projects Using Differential Corrections from Multiple GNSS Fixed Base Stations. *Geocarto International,* Vol. 38(1). https://doi.org/10.1080/10106049.2023.2197507.

[15] Eker, R., Alkan, E. and Aydın, A., (2021). A Comparative Analysis of UAV-RTK and UAV-PPK Methods in Mapping Different Surface Types. *European Journal of Forest Engineering,* Vol. 7(1), 12-25. https://doi.org/10.33904/ejfe.938067.

[16] Žabota, B. and Kobal, M., (2021). Accuracy Assessment of UAV-Photogrammetric-Derived Products Using PPK and GCPs in Challenging Terrains: In Search of Optimized Rockfall Mapping. *Remote Sensing,* Vol. 13. https://doi.org/10.3390/rs13193812.

[17] Stott, E., Williams, R. D. and Hoey, T. B., (2020). Ground Control Point Distribution for Accurate Kilometre-Scale Topographic Mapping Using an RTK-GNSS Unmanned Aerial Vehicle and SfM Photogrammetry. *Drones,* Vol. 4. https://doi.org/10.3390/drones4030055.

[18] Deliry, S. I. and Avdan, U., (2024). Accuracy Assessment of UAS Photogrammetry and Structure from Motion in Surveying and Mapping. *International Journal of Engineering and Geosciences,* Vol. 9(2), 165-190. https://doi.org/10.26833/ijeg.1366146.

[19] Hugenholtz, C., Brown, O., Walker, J., Barchyn, T. E., Nesbit, P., Kucharczyk, M. and Myshak, S., (2016). Spatial Accuracy of UAV-Derived Orthoimagery and Topography: Comparing Photogrammetric Models Processed with Direct Geo-Referencing and Ground Control Points. *Geomatica,* Vol. 70(1), 21-30. https://doi.org/10.5623/cig2016-102.

[20] Varbla, S., Puust, R. and Ellmann, A., (2021). Accuracy Assessment of RTK-GNSS Equipped UAV Conducted As-Built Surveys for Construction Site Modelling. *Survey Review,* Vol. 53(381), 477-492. https://doi.org/10.1080/00396265.2020.1830544.

[21] Alkan, M. N., Aladogan, K., Kose, Z. and Alkan, O., (2020). 2D and 3D Positioning Performance of UAV-Based Photogrammetry in Residential Regions. Hittite Journal of Science and Engineering, Vol. 7(2), 115-123. https://doi.org/10.17350/HJSE19030000180.

[22] Alkan, M. N., (2024). High-Precision UAV Photogrammetry with RTK GNSS: Eliminating Ground Control Points. Hittite Journal of Science and Engineering, Vol. 11(4), 139-147. https://doi.org/10.17350/HJSE19030000341.

[23] Thammaboribal, P., Tripathi, N. and Lipiloet, S., (2026). Comparative Study of UAV Mapping with and without Ground Control Points (GCPs). *International Journal of Geoinformatics,* Vol. 22(3), 36-50. https://doi.org/10.52939/ijg.v22i3.4861.

[24] Chen, K., Reichard, G., Akanmu, A. and Xu, X., (2021). Geo-registering UAV-Captured Close-Range Images to GIS-based Spatial Model for Building Façade Inspections. *Automation in Construction*, Vol. 122. https://doi.org/10.1016/j.autcon.2020.103503.

[25] Vacca, G., Dessì, A. and Sacco, A., (2017). The Use of Nadir and Oblique UAV Images for Building Knowledge. *ISPRS International Journal of Geo-Information,* Vol. 6. https://doi.org/10.3390/ijgi6120393.

[26] Vacca, G., Furfaro, G. and Dessì, A., (2018). The Use of the UAV Images for the Building 3D Model Generation. International Archives of the Photogrammetry, Remote Sensing and Spatial Information Sciences, Vol. XLII-4/W8, 217-223. https://doi.org/10.5194/isprs-archives-XLII-4-W8-217-2018.

[27] Ruiz, R. D. B., Lordsleem Jr., A. C., Rocha, J. H. A. and Irizarry, J., (2022). Unmanned Aerial Vehicles (UAV) as a Tool for Visual Inspection of Building Façades in AEC+FM industry. *Construction Innovation: Information, Process, Management,* Vol. 22(4), 1155-1170. https://doi.org/10.1108/CI-07-2021-0129.

[28] Calisi, D., Botta, S. and Cannata, A., (2023). Integrated Surveying, from Laser Scanning to UAV Systems, for Detailed Documentation of Architectural and Archeological Heritage. *Drones,* Vol. 7. https://doi.org/10.3390/drones7090568.

[29] Zhang, C., Wang, F., Zou, Y., Dimyadi, J., Guo, B. H. W. and Hou, L., (2023). Automated UAV Image-to-BIM Registration for Building Façade Inspection Using Improved Generalised Hough Transform. *Automation in Construction,* Vol. 153. https://doi.org/10.1016/j.autcon.2023.104957.

[30] Zhou, J., Liu, Y., Nie, G., Cheng, H., Yang, X., Chen, X. and Gross, L., (2022). Building Extraction and Floor Area Estimation at the Village Level in Rural China Via a Comprehensive Method Integrating UAV Photogrammetry and the Novel EDSANet. *Remote Sensing,* Vol. 14. https://doi.org/10.3390/rs14205175.

[31] Akay, S. S., Özcan, O., Şanlı, F. B., Bayram, B. and Gorum, T., (2021). Assessing the Spatial Accuracy of UAV-Derived Products Based on Variation of Flight Altitudes. *Turkish Journal of Engineering,* Vol. 5(1), 35-40. https://doi.org/10.31127/tuje.653631.

[32] Barba, S., Barbarella, M., Di Benedetto, A., Fiani, M., Gujski, L. and Limongiello, M., (2019). Accuracy Assessment of 3D Photogrammetric Models from an Unmanned Aerial Vehicle. *Drones,* Vol. 3. https://doi.org/10.3390/drones3040079.

[33] Taddia, Y., González-García, L., Zambello, E. and Pellegrinelli, A., (2020). Quality Assessment of Photogrammetric Models for Facade and Building Reconstruction Using DJI Phantom 4 RTK. *Remote Sensing,* Vol. 12. https://doi.org/10.3390/rs12193144.

[34] Makineci, H. B. and Karasaka, L., (2021). Investigation of 3D Models Acquired with UAV Oblique Images. *Turkish Journal of Geosciences,* Vol. 2(2), 13-20. https://doi.org/10.48053/turkgeo.980559.

[35] Mwangangi, K. K., Mc'Okeyo, P. O., Oude Elberink, S. J. and Nex, F., (2022). Exploring the Potentials of UAV Photogrammetric Point Clouds in Façade Detection and 3D Reconstruction of Buildings. *International Archives of the Photogrammetry, Remote Sensing and Spatial Information Sciences*, Vol. XLIII-B2-2022, 433-440. https://doi.org/10.5194/isprs-archives-XLIII-B2-2022-433-2022.

[36] Cai, D., Chai, S., Wei, M., Wu, H., Shen, N., Zhou, Y., Ding, Y., Hu, K. and Hu, X., (2023). Point Cloud-Based Smart Building Acceptance System for Surface Quality Evaluation. Buildings, Vol. 13, 2893. https://doi.org/10.3390/buildings13112893.

[37] Maraş, E. E. and Nasery, N., (2023). Investigating the Length, Area and Volume Measurement Accuracy of UAV-based Oblique Photogrammetry Models Produced with and without Ground Control Points. *International Journal of Engineering and Geosciences,* Vol. 8(1), 32-51. https://doi.org/10.26833/ijeg.1017176.

[38] Pérez-Portugal, A., Atencio, E., Muñoz-La Rivera, F. and Herrera, R. F., (2023). Calibration of UAV Flight Parameters to Inspect the Deterioration of Heritage Facades Using Orthogonal Arrays. *Sustainability,* Vol. 15. https://doi.org/10.3390/su15010232.

[39] The New DJI Mavic 3 Enterprise Series Sets Ultimate Standard for Portable Commercial Drones. DJI. [Online]. Available: https://www.dji.com/media-center/announcements/the-new-dji-mavic-3-enterprise-series-sets-ultimate-standard-for-portable-commercial-drones. [Accessed: Apr. 21, 2026].

[40] Specs - DJI Mavic 3 Enterprise. DJI Enterprise. [Online]. Available: https://enterprise.dji.com/mavic-3-enterprise/specs. [Accessed: Apr. 21, 2026].

[41] Professional Photogrammetry and Drone Mapping Software. Pix4D. [Online]. Available: https://www.pix4d.com/. [Accessed: Apr. 21, 2026].

[42] Agisoft Metashape. Agisoft. [Online]. Available: https://www.agisoft.com/. [Accessed: April 21, 2026].

[43] 3DF Zephyr - Photogrammetry Software - 3D Models from Photos. 3Dflow. [Online]. Available: https://www.3dflow.net/3df-zephyr-photogrammetry-software/. [Accessed: Apr. 21, 2026].

[44] Nurunnabi, A., Belton, D. and West, G., (2014). Robust statistical approaches for local planar surface fitting in 3D laser scanning data. ISPRS Journal of Photogrammetry and Remote Sensing, Vol. 96, 106-122. https://doi.org/10.1016/j.isprsjprs.2014.07.004.

[45] Shapiro, S. S. and Wilk, M. B., (1965). An Analysis of Variance Test for Normality (complete samples). *Biometrika,* Vol. 52(3-4), 591-611. https://doi.org/10.1093/biomet/52.3-4.591.

[46] Wilcoxon, F., (1945). Individual Comparisons by Ranking Methods. *Biometrics Bulletin,* Vol. 1(6), 80–83. https://doi.org/10.2307/3001968.

[47] Xu, M., Fralick, D., Zheng, J. Z., Wang, B., Tu, X. M. and Feng, C., (2017). The Differences and Similarities Between Two-Sample T-Test and Paired T-Test. *Shanghai Archives of Psychiatry*, Vol. 29(3), 184-188. https://doi.org/10.11919/j.issn.1002-0829.217070.

[48] Wessel, P., Luis, J. F., Uieda, L., Scharroo, R., Wobbe, F., Smith, W. H. F. and Tian, D., (2019). The Generic Mapping Tools Version 6. Geochemistry, Geophysics, Geosystems, Vol. 20(11), 5556–5564. https://doi.org/10.1029/2019GC 008515.